J Mater Sci: Mater Electron **(2024) 35:1017**

البحث الخامس فى قائمة الابحاث المقدمة للترقية (رقم ٢٥ فى القائمة الرئيسية)   (5)

From experimentation to prediction: comprehensive study of dielectric properties through experimental research and theoretical modeling

H. I. Lebda[1,*], H. E. Atyia[1], and D. M. Habashy[1]

[1] *Faculty of Education, Physics Department, Ain Shams University, Roxy, Cairo 11771, Egypt*

Received: 5 March 2024
Accepted: 9 May 2024

ABSTRACT

This study discusses the experimental findings on the frequency & temperature influences on the dielectric (constant (ε$_1$) and loss (ε$_2$)) of some chalcogenide materials based on $Se_{83}Bi_{17}$ composition performed in the temperature range 303 K–393 K and frequency range (100–1000000 Hz). As the frequency increases, multiple polarization mechanisms contribute to the reduction of the dielectric constant. The addition of germanium (Ge) to a composition increases ε$_1$ more than tellurium (Te). The dielectric loss decreases with frequency while increasing with temperature and AC conductivity. Understanding these behaviors is important for material characterization and applications in fields like electronics and solar cells. The theoretical section introduces adaptive neuro-fuzzy inference systems (ANFIS), which are utilized in the estimation of the dielectric characteristics of $Se_{83}Bi_{17}$ (SB), $Se_{83}Bi_{17}Te_5$ (SB-T), and $Se_{83}Bi_{17}Ge_5$ (SB-G). Experimentation-related data are a source of input. ANFIS model of the Takagi–Sugeno type has been trained. With MATLAB, the most effective networks are created. The outcomes of the ANFIS modeling are exceptional. The accuracy of the modeling process is due to the error values. This study demonstrates that the ANFIS technique can accurately anticipate the dielectric properties of the compositions under consideration when they are formed into thin films. The ANFIS can describe the experimental data of the dielectric (constant (ε$_1$) and loss (ε$_2$)) of some chalcogenide materials for all the mentioned temperatures and frequencies. This leads to using the ANFIS model to produce the dielectric (constant (ε$_1$) and loss (ε$_2$)) of some chalcogenide materials for various temperatures and frequencies which there are no experimental data yet to compare with.

1 Introduction

Understanding the electrical behavior of materials heavily relies on the examination of dielectric properties, including the dielectric constant & loss tangent. These properties are particularly important in the field of electronics and telecommunications, where efficient transmission and storage of electrical signals are essential. The choice of these compounds is based on their unique properties and potential applications

---

https://doi.org/10.1007/s10854-024-12746-7

in electronic devices. Selenium-based compounds are known for their semiconducting behavior, while bismuth exhibits interesting electrical properties, including a low carrier density and high mobility. The addition of germanium and tellurium further modifies the material's characteristics, allowing for a wider range of applications. To determine the insulation properties of these compounds, we will focus on two key parameters: insulation constant and loss tangent. The dielectric constant, also known as the relative permittivity, measures the ability of a material to store electrical energy. It is a dimensionless quantity that compares the capacitance of a material with that of a vacuum. A higher dielectric constant indicates a higher ability to store electrical energy. The loss tangent, on the other hand, represents the energy lost as heat during the electrical polarization of a material. It is the tangent of the angle between the electrical loss and the energy storage components of the complex permittivity. A low-loss tangent indicates a material with minimal energy loss and is desirable for efficient signal transmission. To conduct our study, we will employ various experimental techniques, including capacitance measurements and impedance spectroscopy. These methods allow us to characterize the electrical behavior of the compounds over a range of frequencies, providing insights into their insulation properties. By examining the dielectric constant and dielectric loss of Se83Bi17, Se83Bi17Ge5, and Se83Bi17Te5, we aim to gain a deeper understanding of their suitability for electronic applications. The results of this study will contribute to the advancement of materials science and facilitate the development of new technologies in the field of electronics and telecommunications [1–10]. An ANFIS model includes the benefits of fuzzy logic (FL) and artificial neural networks (ANN) to maximize the advantages of both approaches. The ANFIS model is distinguished by a self-learning process that optimizes control rules and demonstrates human-like reasoning abilities. Numerous studies have recently been used that rely on the ANFIS model to predict various properties of physics [11–31]. The modeling research despite its impotence, a comprehensive study of dielectric properties using ANFIS remains lacking. The important goal of the study is to obtain a precise and effective method for forecasting dielectric properties. To accomplish the goal, the ANFIS model utilizes the experimental data as inputs. It is anticipated that after the process of simulation is finished, high-accuracy rules and results connecting inputs and outputs will be achieved. By doing so, it will be possible to predict results for which experimental measurements have not yet been made. Using ANFIS to model the dielectric properties is the contribution of this paper.

Four sections make up the research. Background details and the main idea are presented in the first section. The second section discusses the fundamentals of sample preparation, characterization, and the ANFIS model and explains how the ANFIS model is processed. The results are presented, explained, and compared between the experimental data and results of the ANFIS in the third section. The main points of the paper's accomplishments are summarized in the fourth section.

2 Sample preparation, characterization, and theoretical characterization techniques

2.1 Preparation and characterization of samples

The melt-quench method [32]. Although there are other ways to make glasses, the melt quenching process is the most preferred since it is quicker and less expensive than other procedures. A liquid must typically be rapidly cooled below its freezing point to become glass, and this is commonly regarded as one of the criteria for defining a glassy state. The traditional definition of glass formation is the process by which a molten sample (i.e., a liquid that forms glass) is quickly cooled, its fluidity diminishes until it virtually zeroes out at a specific temperature below the freezing point. The glass samples of the compositions $Se_{83}Bi_{17}$ (SB), $Se_{83}Bi_{17}Te_5$ (SB-T), and $Se_{83}Bi_{17}Ge_5$ (SB-G) were made using the melt-quench process. Se, Bi, Te, and Ge (Sigma-Aldrich) were utilized as starting ingredients because of their high purity (99.99%). The mentioned high-purity chemicals were estimated and weighed in a batch of 5-g powder form, then enclosed in quartz ampoules with a vacuum of 10^{-5} Torr. After that, an oscillating furnace was used to raise the ambient temperature of the sealed ampoules by approximately 3 K per minute up to 1273 K. The ampoules were placed at these temperatures for 18 h while still being regularly rocked to obtain a homogeneous. The melt was then abruptly cooled with ice water to achieve a glassy form. To obtain bulk samples, break the silica ampoules. A pestle and mortar was used

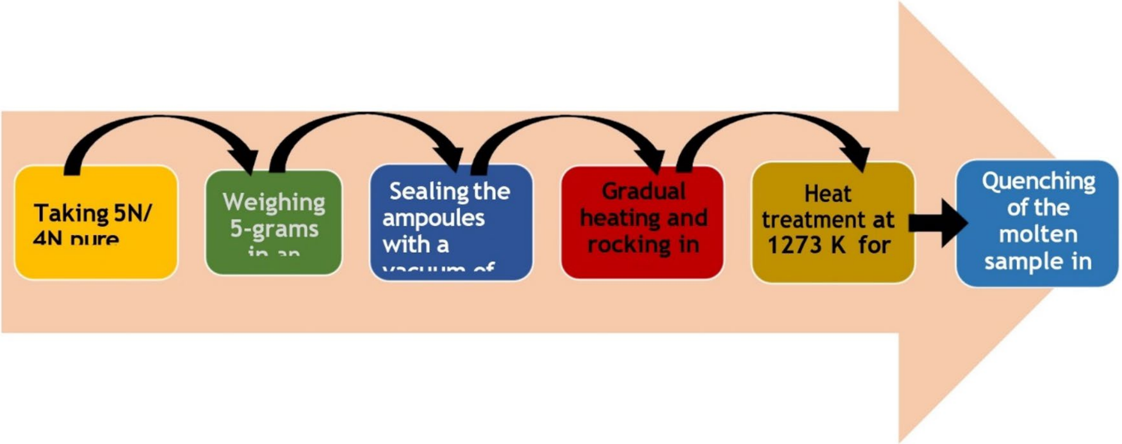

Fig. 1 Schematic diagram for the process of different bulk samples of glassy $Se_{83}Bi_{17}$ (SB), $Se_{83}Bi_{17}Te_5$ (SB-T), and $Se_{83}Bi_{17}Ge_5$ (SB-G)Se by melt quenching method

to create a fine powder. Figure 1 shows the graphic illustration of the melt-quench procedure. Physical vapor deposition was used to create the amorphous thin films of the bulk samples at a low vacuum (10^6 torr). The deposition region was a square with a side of 2 mm, and the thin film was around 400 nm thickness. A quartz crystal thickness monitor is utilized to regulate the thickness of these films during the deposition process. For measurements of film thickness, the experimental errors are 2%. Dielectric measurements were conducted on a thin film, and its thickness was determined to be 400 nm. The thin film samples were placed between two aluminum electrodes, one below and one above. To measure the sample's capacitance (C) and loss tangent (tan δ), a programmable automatic bridge (RLC PM 6304, Phillips) was employed. The measurements were performed in the temperature range 303 K–393 K with a heating rate of 10, and frequency range (100–1000000 Hz) for the investigated $Se_{83}Bi_{17}$ (SB), $Se_{83}Bi_{17}Te_5$ (SB-T), and $Se_{83}Bi_{17}Ge_5$ (SB-G) film samples. It should be noted that all the film samples studied on the bridge screen were represented as parallel capacitance (C) and resistance (R). The dielectric constant (ε_1) and dielectric loss were determined using the following equations: $\varepsilon = C\ \varepsilon_0 / t\ A$ and $\varepsilon_2 = \varepsilon_1$ (tan δ), where t represents the film thickness, A is the film cross-section area, and ε_0 denotes the permittivity of free space. The phase angle (ϕ) was used to calculate $\delta = (90–\phi)$ [33]. All experimental data lines in the figures were fitted using the least square method [34, 35]. The temperature of the system was regulated using an electronic temperature controller attached to the cell. The temperature measurements were facilitated by a chromel alumel thermocouple placed near the sample. The temperature dependence of the dielectric constant and dielectric loss was investigated by uniformly increasing the temperature at a rate of 50 in the range from 305 to 358 K.

Using EDX spectroscopy, the compositions of SB, SB-T, and SB-G thin films were investigated. The percentages of their constituent parts that were found are roughly equivalent to those of the synthetic compositions devoid of any impurities. Figure 2 displays the XRD patterns of the chalcogenide films that were studied at RT. These trends demonstrate that the absence of crystalline peaks verifies that the SB, SB-T, and SB-G film samples are in an amorphous state.

2.2 Theoretical characterization techniques

2.2.1 *ANFIS model: architectures, learning algorithm, and membership functions.*

ANFIS was created in 1992 by J.S. Roger Jang. The ANFIS is an innovative form that combines neural networks and fuzzy logic [36]. The ANFIS is an example of a multilayer feedforward network [37]. The ANFIS creates a FIS by optimizing the membership function parameters using a NN. As indicated by Tarno et al. [37], the FIS will be able to differentiate between the four kinds of membership functions (MFs) offered by the ANFIS: triangle, trapezoidal, Generalized Bell, and Gaussian. ANFIS provides a tool for optimizing the MF parameters in the fuzzy model for the given

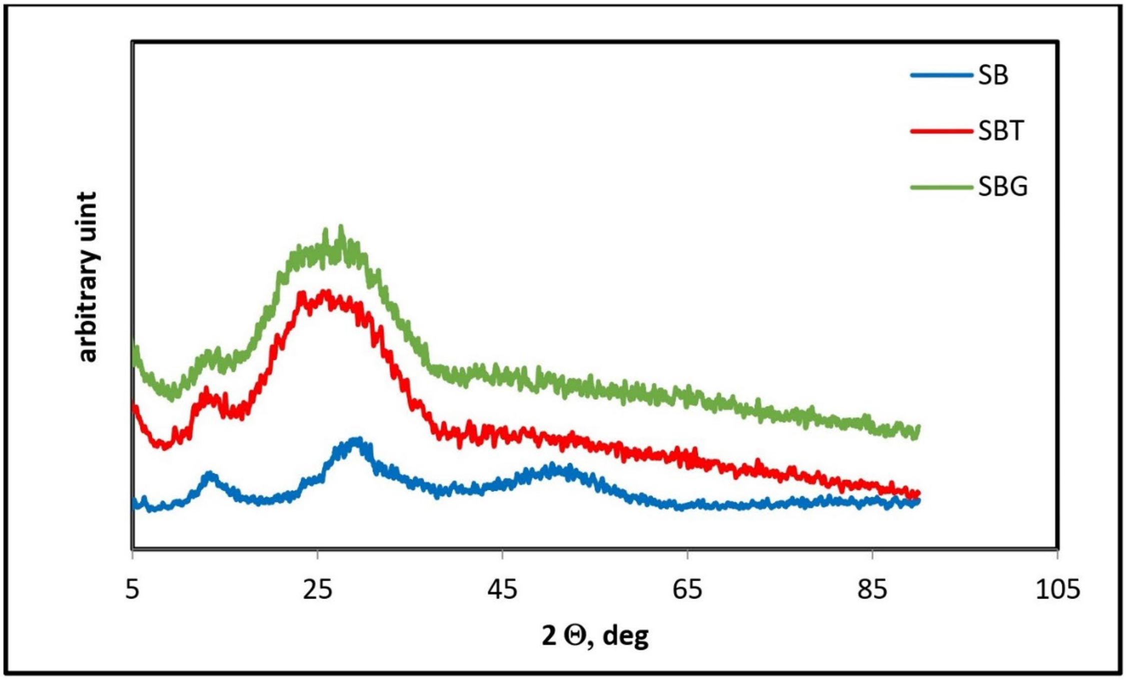

Fig. 2 X-Ray diffraction pattern for a $Se_{83}Bi_{17}$ (SB), $Se_{83}Bi_{17}Te_5$ (SB-T), and $Se_{83}Bi_{17}Ge_5$ (SB-G) films with thickness ~ 400 nm

dataset. The ANFIS applies learning techniques such as a hybrid, and a backpropagation algorithm.

2.2.2 *ANFIS architecture*

Figure 3 depicts the ANFIS standard architecture. The ANFIS, for illustration, has one output (*f*) and two inputs (*x*, *y*). Assume the following Takagi and Sugeno [14] fuzzy if–then rules.

(1) If x is A_1 and y is B_1, then $f_1 = a_1x + b_1y + r_1$,

(2) If x is A_2 and y is B_2, then $f_2 = a_2x + b_2y + r_2$,

where the linear parameters are a_1, a_2, b_1, b_2, r_1, r_2, and the nonlinear parameters are A_1, A_2, B_1, B_2.

The following describes each layer of Fig. 3.

2.2.2.1 The first layer (the fuzzy layer) The nodes in the first layer i are all adaptive nodes, with the following node function, which is given by Eq. (2),

$$O_{1,i} = \mu_{A_i}(x), \tag{1}$$

Fig. 3 ANFIS architecture

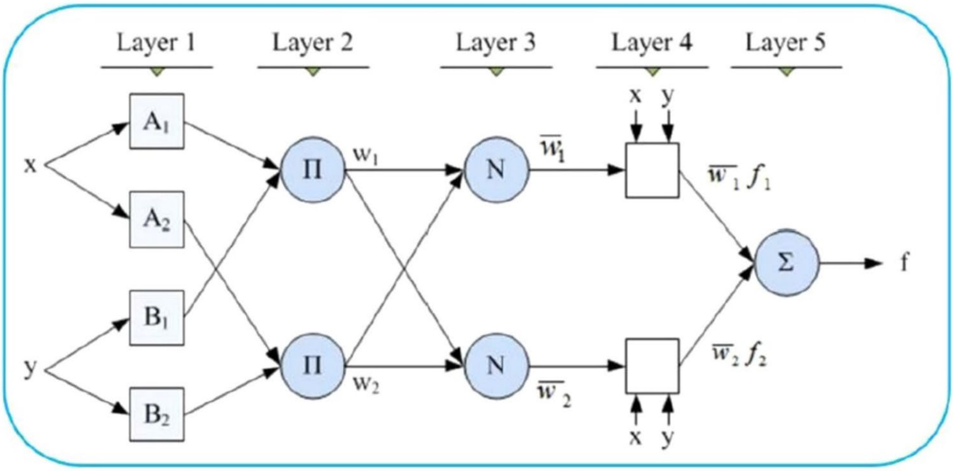

where $O_{1,i}$ is the i-th node's output and $\mu_{A_i}(x)$ is the degree of MF.

2.2.2.2 *The second layer (Product Layer)*

Each node in the 2nd layer is a circular node that multiplies the approaching signal. In this phase, the fuzzy AND operator is used to extract the product. As shown in Eq. (2),

$$w_i = \mu_{A_i}(x) \times \mu_{B_i}(x), \cdots\cdots i = 1,\ 2 \quad (2)$$

here, w_i denotes the firing strength of the i-th rule, $\mu_{A_i}(x)$ and μ_{B_i} denote the degree of MF fuzzy sets A_i and B_i.

2.2.2.3 *The third layer (Normalized Layer)*

The nodes in the 3rd layer are all circular. It will be established in the third layer by normalized firing strengths, that is obtained by division of the firing strength for each rule by the total rules number, as illustrated in Eq. (3), this step's output is the normalized firing strength.

$$\overline{w}_1 = \frac{w_1}{w_1 + w_2},\ i = 1,\ 2 \quad (3)$$

2.2.2.4 *The fourth layer (the de-fuzzy layer)*

The nodes in 4th layer are all square, additionally referred to as flexible nodes. To calculate the outcome of this stage, use the following function. As shown in Eq. (4),

$$\overline{w_i}f_i = \overline{w_i}\left(p_i x + q_i y + r_i\right), i = 1, 2 \quad (4)$$

here, $\overline{w_i}$ is a normalized firing strength of layer three, and f_i is an ANFIS outcome. x and y are ANFIS inputs, and $\{p_i, q_i, r_i\}$ is the parameters set (consequent parameters).

2.2.2.5 *The fifth layer (Total Output Layer)*

A single node in the 5th layer will add up each of the signals that come from the layer before computing output overall, as illustrated in Eq. (5),

$$overall\ output = \sum_i \overline{w_1}f_i = \frac{\sum_i w_i f_i}{\sum_i w_i}, i = 1, 2 \quad (5)$$

2.2.3 *Learning algorithm of ANFIS*

The ANFIS learning method includes modifying the MF's parameter set to obtain the optimal solutions and parameters [37]. This method of optimization is a modification of the premise and its resulting parameters. The settings are changed to minimize the error, which will be determined as the square root of the sum of the output and observation value differences. This study is going to employ the hybrid algorithm. Jang [38] claims in the ANFIS that the hybrid learning technique is more efficient. A hybrid algorithm mixes the least squares and backpropagation approaches. According to Jang [38], the hybrid approach requires the premise parameters to first backward pass the network before moving forward pass it. The least square algorithm determines the subsequent parameters when the input is transmitted to layer 4. Another method for determining premise parameters is backward step gradient descent.

2.2.4 *Membership functions (MFs)*

In fuzzy set theory, a MF determines the degree of truth of a crisp value between of zero and one [39]. Depending on how the curve is shaped, each MF has a different name, such as triangular, bell-shaped, trapezoidal, or Gaussian membership functions. Figure 4 shows examples of the basic types of MFs. The Trapezoidal Membership Function (Trapmf) has a truncated triangle shape, the generalized bell-shaped membership function (Gbellmf) has a bell-like symmetrical form, the most fundamental form is the triangle membership function (Trimf), which has a triangle curve, and Gaussian membership function (Gaussmf) has a smooth curve, identical to bell-shaped MF.

2.2.5 *Forecasting and evaluating the performance*

ANFIS performance with various partitioning methods and MFs are assessed using Mean Absolute Error (MAE), Mean Square Error (MSE), Root Mean Square Error (RMSE), correlation coefficient ($R.^2$), mean error $\overline{e_i}$, and standard deviation (STd) [40] as shown in Eqs. (6–12)

$$e_i = \left(O_i - T_i\right) \quad (6)$$

$$\overline{e_i} = \sum_{t=1}^{n} \left(O_i - T_i\right)/n \quad (7)$$

$$MSE = \sum_{t=1}^{n} \left(O_i - T_i\right)^2/n \quad (8)$$

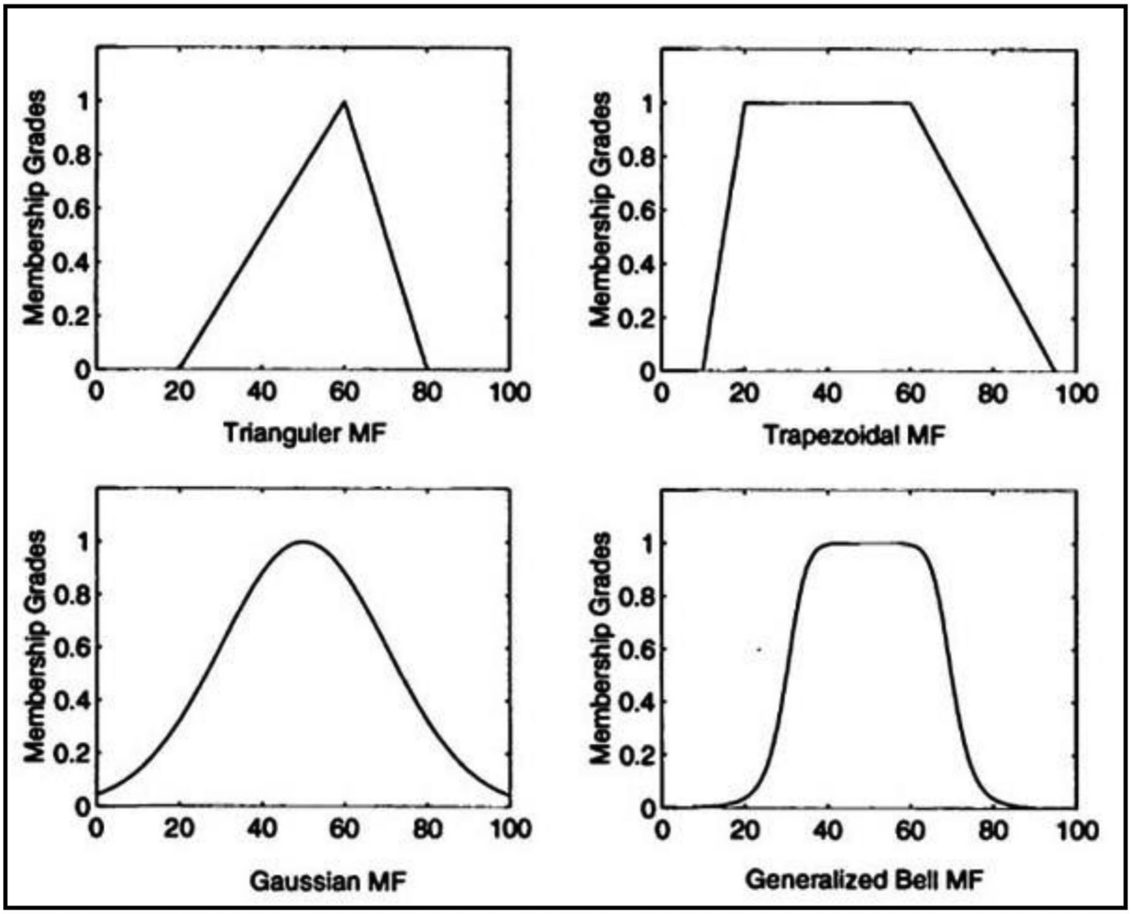

Figure. 4 Basic shapes of membership functions

$$STd = \left(\frac{1}{n-1} \sum_{i=1}^{n} \left(e_i - \overline{e_i} \right)^2 \right)^{1/2} \tag{9}$$

$$RMSE = \left(\frac{1}{n} \sum_{i=1}^{n} \left(O_i - T_i \right)^2 \right)^{1/2} \tag{10}$$

$$R^2 = 1 - \left(\frac{\sum_i \left(O_i - T_i \right)^2}{\sum_i \left(O_i \right)^2} \right) \tag{11}$$

$$MAE = \sum_{i=1}^{n} \left| O_i - T_i \right| / n. \tag{12}$$

here, O_i, n, and T_i provide the experimental objective, data points, and model's outcome, respectively.

3 Results with discussions

3.1 Frequency and temperature influences on dielectric constant ε_1: experimental discoveries

Dielectric analysis is a technique used to evaluate the electrical properties of a material by varying temperature and frequency. It assesses two fundamental electrical characteristics: capacitance, which indicates the material's ability to store electrical charge, and conductivity, which represents its capacity to conduct electricity. By conducting dielectric analysis, one can obtain information about a material's dielectric constant (ε_1), dielectric loss (ε_2), and dielectric loss tangent or dissipation factor (tan δ). The dielectric dispersion, which refers to the distribution of relaxation time induced by polarization species, can also be examined. Additionally, studying the temperature and frequency dependence of dielectric parameters, particularly in the low-frequency range where dielectric dispersion occurs, is crucial for understanding losses that occur in these materials. Figure 5a–c displays plots depicting the relationship between the dielectric constant (ε_1) and frequency at different temperatures for glassy thin films of $Se_{83}Bi_{17}$ (SB), $Se_{83}Bi_{17}Te_5$ (SB-T), and $Se_{83}Bi_{17}Ge_5$ (SB-G), samples, respectively.

As shown in Fig. 6, by analyzing the given data, it becomes apparent that both ε_1 and ε_2 exhibit a decline as the audio frequency rises. The decrease in the dielectric constant at higher frequencies can be explained by the engagement of different polarization mechanisms [41, 42] within polar materials, namely electronic polarization (Pe), ionic polarization, dipolar polarization (Pd), and space charge polarization (Ps). Electronic polarization, which stems from the displacement of valence electrons in relation to the positive nucleus, remains the primary contributor up to frequencies of 10^{16} Hz. Ionic polarization occurs when positive and negative ions are displaced from each other and can be observed at frequencies up to a maximum of 1013 Hz. Dipolar polarization arises due to the presence of molecules possessing permanent electrical dipole moments, which can align with the direction of the applied electric field, and is observed at frequencies up to approximately 1010 Hz. Lastly, space charge polarization occurs due to the impedance of mobile charge carriers at interfaces, taking place between frequencies of 1 and 10^3 Hz. The overall polarization of a dielectric substance can be calculated as the cumulative effect of these four types. However, the current study indicates that ionic polarization has minimal influence on the overall polarization, which aligns with the expected behavior given the covalent nature of the compositions being investigated. Equation (13) [43] can be utilized to estimate the extent of covalence in the studied compositions.

$$\text{The proportion of covalent character} = 100\% \exp(-0.25(c_A - c_B)^2), \tag{13}$$

where A and B represent the electronegativities of atoms A and B, respectively. Table 1 provides the corresponding values for the covalent character. As the frequency of the applied field increases, the dipoles' ability to rotate rapidly decreases, causing a lag between their oscillations and those of the field. Consequently, the dipole's capacity to completely align with the field diminishes as the frequency rises, resulting in a decline in orientation polarization. This leads to a decrease in ε, eventually approaching a constant value at higher frequencies due to interfacial or space charge polarization.

Figure 5a–c shows the increase of ε_1, with temperature at different frequencies. This behavior can be attributed to the fact that the dipoles in polar materials [44] cannot orient themselves at low temperatures. When the temperature is increased the dipoles attain some freedom, i.e., the orientation of dipoles is facilitated and thus increases the value of the orientation polarization, which increases ε_1. As observed in Fig. 5a–c, the values of ε_1 have been increasing with Ge and Te addition to the Se–Bi binary composition, which can be understood in terms of the bonding nature between the constituent elements in the investigated composition. Taking a closer look at the results, it can be observed that with the addition of Ge the increase is higher than that for Te addition. The bond energy between the host element Se and Ge is greater compared to that between Se and the other additive, Te atoms. This means that the network structure contains stronger Se–Ge bonds, which are more sensitive to an electric field than the stronger bonds. Thus, the value of ε_1 decreases as a behavior trend ($Se_{83}Bi_{17}$ (SB)) < ($Se_{83}Bi_{17}Te_5$ (SB-T)) < ($Se_{83}Bi_{17}Ge_5$ (SB-G)) for the studied film samples.

The correlation between the dielectric constant and AC conductivity can be described by a novel parameter, denoted as M (the figure of merit), as shown in Eq. (14), which is associated with the response time. Materials with higher values of parameter M are deemed more suitable for solar cell applications [45].

$$M = \sigma_{ac}/\varepsilon_1 \tag{14}$$

Table 2 presents the values of M for the examined film samples at different temperatures. It is evident that the parameter exhibits the following trend: ($Se_{83}Bi_{17}$ (SB)) < ($Se_{83}Bi_{17}Te_5$ (SB-T)) < ($Se_{83}Bi_{17}Ge_5$ (SB-G)), and decreases as the temperature increases.

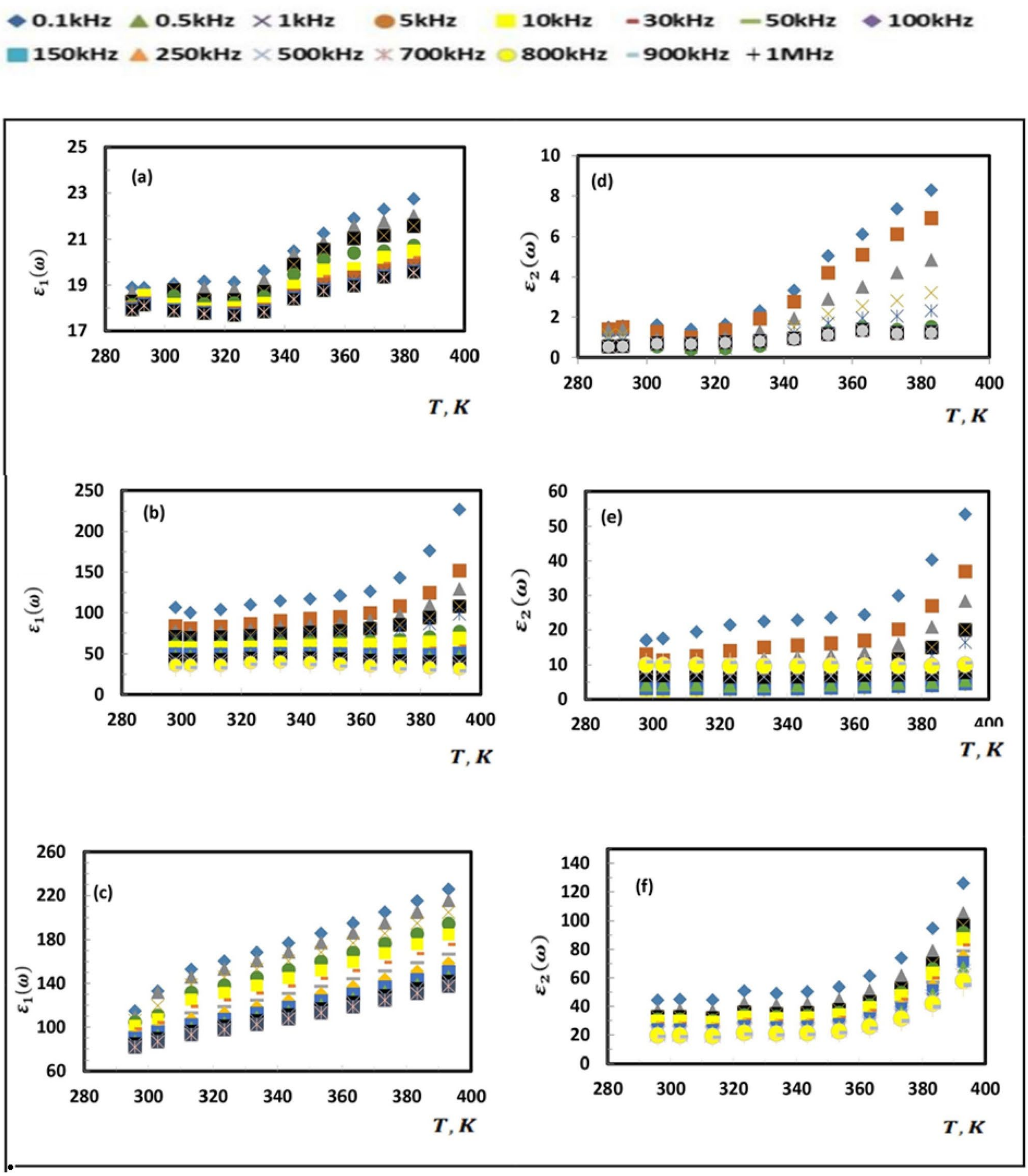

Fig. 5 dielectric constant (ε_1) (**a**, **b**, **c**) and dielectric loss (ε_2) (**d**, **e**, **f**), respectively, as a function of temperature for glassy thin films thin films of $Se_{83}Bi_{17}$ (SB), $Se_{83}Bi_{17}Te_5$ (SB-T), and $Se_{83}Bi_{17}Ge_5$ (SB-G) samples, respectively, as a function of frequency

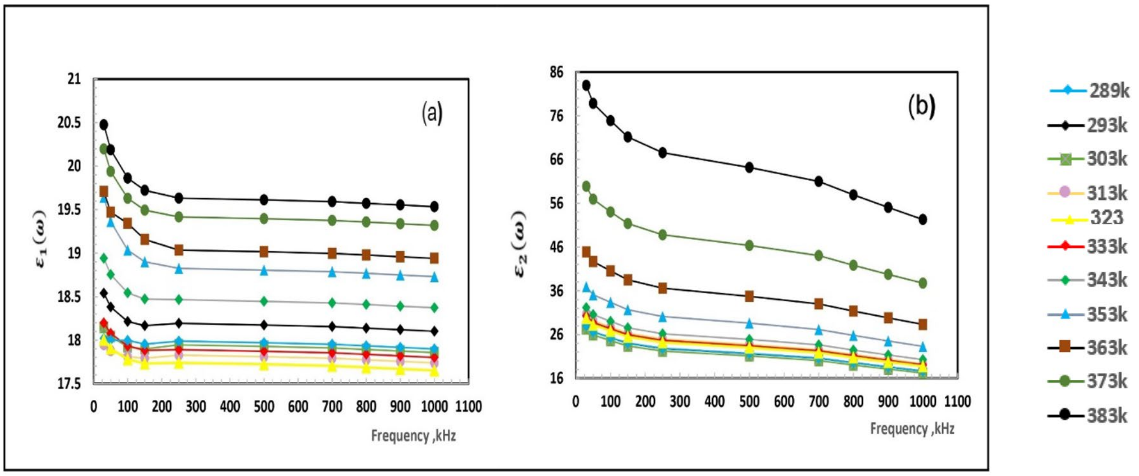

Fig. 6 **a** the dielectric constant (ε_1) for glassy thin films of $Se_{83}Bi_{17}$ (SB), **b** the dielectric loss (ε_2) for glassy thin films of $Se_{83}Bi_{17}Ge_5$ (SB-G) vs frequency at different temperatures

Table 1 Calculated covalent character of bonds for the investigated $Se_{83}Bi_{17}$ (SB), $Se_{83}Bi_{17}Te_5$ (SB-T), and $Se_{83}Bi_{17}Ge_5$ (SB-G) film samples

Bonds for bond type	% covalent character
Se–Se	100
Se–Te	96
Se–Ge	93
Se–Bi	94
Te–Bi	99.8
Te–Te	100
Ge–Ge	100
Ge–Bi	99.9

Table 2 Values of the figure of merit parameter M for the studied film composition

Film composition	The figure of merit parameter $M \times 10^{-7}$			
	303K	323K	343K	373K
SB	0.89	0.71	0.70	0.62
SB–Te	1.01	1.00	0.92	0.83
SB–Ge	1.31	1.26	1.13	1.10

3.2 Frequency and temperature-dependent behavior of dielectric loss ε_2: experimental findings

The frequency dependence of the dielectric loss, represented by ε_2, was investigated for various temperatures in the studied film compositions with a thickness of 400 nm. The results are illustrated in Fig. 5d–f.

It was observed that ε_2 decreases as the frequency increases. This can be explained by considering the ions migration within the glass, which is the primary cause of dielectric loss at lower frequency values. The frequency dependence of the dielectric constant (ε_1) and dielectric loss (ε_2) at different temperatures is shown in Fig. 6a, b for glassy thin films of $Se_{83}Bi_{17}$ (SB) and $Se_{83}Bi_{17}Ge_5$ (SB-G), respectively. This phenomenon can be attributed to the decrease in ε_2 as the frequency increases. At low and intermediate frequencies, the dielectric loss is characterized by high values due to the contribution of ion jump, conduction loss resulting from ion migration, as well as ion polarization loss. However, at high frequencies, the ion vibrations become the sole source of dielectric loss, leading to a decrease in ε_2. Furthermore, the figures demonstrate that ε_2 increases as the temperature rises, along with the increase in σ_{ac}/ω [46, 47]. Consequently, as temperatures rise, the AC conduction loss also experiences an increase. At lower temperatures, the losses related to conduction, dipoles, and vibrations are minimized. However, as the temperature rises, these losses start to impact the dielectric loss as well. [48–50]

3.3 Theoretical analysis

This study aims to model, simulate, and predict the dielectric (constant (ε_1) and loss (ε_2)) at various frequencies for glassy thin films of $Se_{83}Bi_{17}$ (SB), $Se_{83}Bi_{17}Te_5$ (SB-T), and $Se_{83}Bi_{17}Ge_5$ (SB-G) samples, respectively, as a function of temperatures. The system was trained on contexts from various scenarios using experimental data to identify the best-optimized ANFIS system performance. To complete the modeling process and find the best fuzzy configuration, six ANFIS networks were designed. The first three ANFIS networks for $\varepsilon_1 (\omega)$ and the second three ANFIS networks for $\varepsilon_2 (\omega)$ at different frequencies as a function of temperature T (K), respectively.

The data were split into two distinct sets: the training set of data, which comprised 80% of the dataset, and the checking dataset, which comprised 20% of the dataset. The ANFIS model was trained through the training set of data. The checking set of data was utilized to validate the trained ANFIS model's accuracy and efficiency. The ANFIS model is fed with experimental data. MATLAB (R2017 a) was used to process the modeling. The ANFIS model was trained with different rules, MFS types, MFs numbers, and epoch numbers before determining the architecture with the lowest RMSE. The Sugeno-type ANFIS model is used in this work. Two input parameters (Temperature and Frequency) and one output parameter (the dielectric constant $\varepsilon_1 (\omega)$ for the first three networks and dielectric loss $\varepsilon_2 (\omega)$ for the second three networks) for glassy thin films of $Se_{83}Bi_{17}$ (SB), $Se_{83}Bi_{17}Te_5$ (SB-T), and $Se_{83}Bi_{17}Ge_5$ (SB-G) samples. In the ANFIS to optimize the output parameter, the Hybrid Method is used. The type and number of MFs are both critical in the development of the ANFIS architecture. All of the networks were trained on all inputs using eight different MFs: Trimf, Trapmf, Gbellmf, Gaussmf, Gauss2mf, Pimf, Dsigmf, and Psigmf, with linear as well as constant output MF. As shown in Fig. 7, the number of MFs is (6*6), and 36 (6^2) rules can be generated with six fuzzy sets for each variable. To determine the appropriate type and number of MFs, trials and error values are used, as well as optimization method types, to create the ANFIS model as shown in Fig. 8.

Table 3 describes and highlights the traits and requirements for the ideal ANFIS networks. The best ANFIS networks are discovered to share several traits. They are of the Takagi–Sugeno type and employ the defuzzification technique weight average (Wtaver), and have 101 nodes, 108 linear parameters, 36 nonlinear parameters, 144 total parameters, and 100 training epochs, for each optimal ANFIS network. Tables 4–5 show the RMSE of various network architectures using the eight types of input MFs on both training and checking datasets, and linear and constant MF for output parameter is used to develop the ANFIS model. As we can see, the RMSE values obtained by using the linear output mf are all less than those obtained by using the constant output mf, and show that the Gaussian (gaussmf) membership function performs most effectively with the lowest RMSE during validation with maximum epoch numbers 100, and Table 6 sums up RMSE, MSE, MAE, R^2 value, $\overline{e_i}$, and Std error. Figure 9 shows the surface viewer results, illustrating how the two inputs have an impact on the output; Fig. 9a–c for dielectric constant (ε_1), Fig. 9d–f

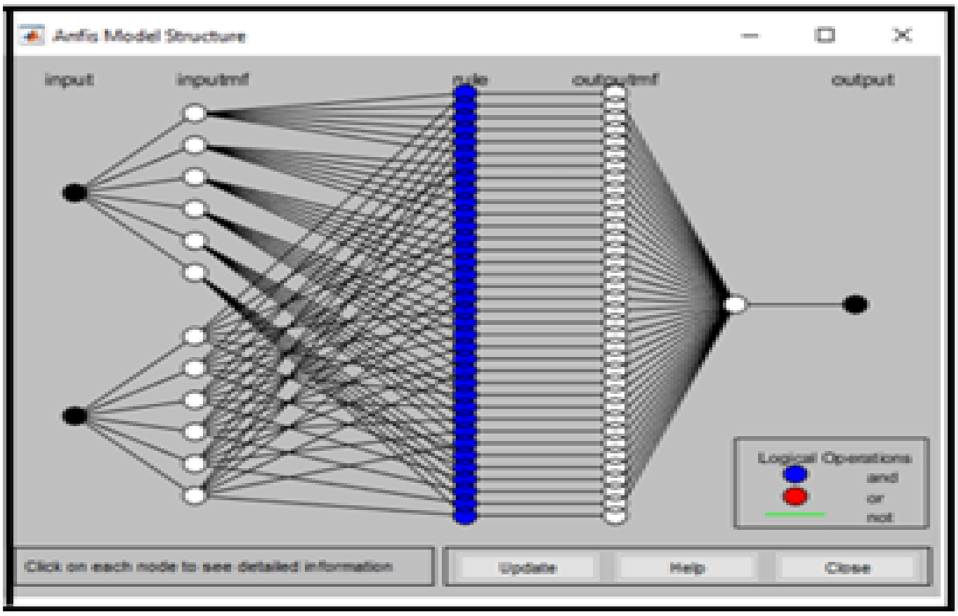

Click on each node to see detailed information

Fig. 7 The ANFIS model structure

Fig. 8 Fuzzy role architecture of the Gaussian membership function

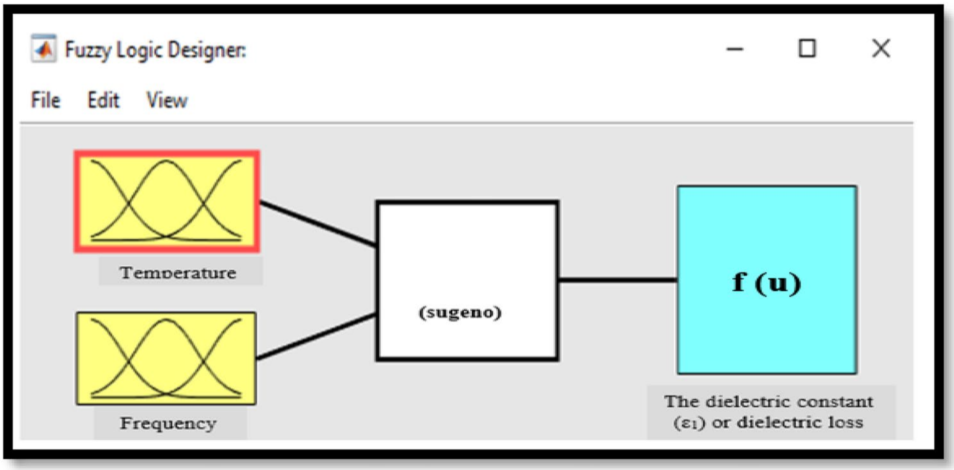

Table 3 ANFIS optimal characteristics

Result ANFIS Modeling	Results
Fuzzy structure	Sugeno type
Defuzzification method	Wtave
Basic FIS for training	Genfis1
No. of MFs for each input	06-Jun
MF Type—inputs	Gaussmf
No. of nodes	101
No. of linear parameters	108
No. of nonlinear parameters	24
Total number of parameters	132
Epoch	100
MF Type—Output	Linear
Training algorithm	Hybrid
No. of inputs	2
Number of output MFs	36
Number of fuzzy rules	36

for dielectric loss (ε_2), respectively, as a function of temperature T (K) & different frequencies (kHz) for glassy thin films of $Se_{83}Bi_{17}$ (SB), $Se_{83}Bi_{17}Te_5$ (SB-T), and $Se_{83}Bi_{17}Ge_5$ (SB-G) samples, respectively. Figure 10 illustrates a visual representation of the prediction's accuracy. Measured data are shown by blue dots, while ANFIS model outputs are indicated by red asterisks. Figure 10a–c for dielectric constant (ε_1), and Figure 10d–f for dielectric loss (ε_2) comparing the results of the ANFIS with the experimental data. The results of the ANFIS modeling are shown in Fig. 11. Solid line curves are used to symbolize the simulation ANFIS findings. Symbols are used to symbolize the experiment's findings. Also shown are dashed lines, which indicate the anticipated ANFIS outcomes. It was discovered that the experimental data symbols and the simulation ANFIS curves matched, suggesting excellent simulation performance. The processing includes

Table 4 Performance of different models under various MF types for the dielectric constant (ε_1)

	Network 1				Network 2				Network 3			
Output MFs	Constant		Linear		Constant		Linear		Constant		Linear	
Inputs MFs	Train	Check	Train	Check	Train	Check	Train	Check	Train	Check	Train	Check
Trimf	0.018	0.03	0.098	0.142	0.027	0.043	0.593	0.76	0.137	0.224	1.666	2.29
Trapmf	0.03	0.053	0.119	0.187	0.17	0.306	0.997	1.473	0.779	1.417	2.467	4.361
Gbellmf	0.019	0.034	0.103	0.163	0.074	0.09	0.748	1.059	0.154	0.267	1.864	3.183
Gaussmf	0.017	0.029	0.099	0.154	0.022	0.026	0.714	1.063	0.072	0.109	1.911	3.137
Gauss2mf	0.024	0.042	0.117	0.187	0.115	0.181	1.03	1.537	0.547	0.615	2.563	4.54
Pimf	0.031	0.055	0.135	0.209	0.178	0.322	1.198	1.753	0.76	1.387	3.054	5.228
Dsigmf	0.022	0.038	0.104	0.148	0.1	0.167	0.608	0.406	0.289	0.445	1.219	1.62
Psigmf	0.021	0.037	0.097	0.139	0.167	0.148	0.608	0.403	0.137	0.224	1.666	2.29

Table 5 Performance of different models under various MF types for dielectric loss ε_2

	Network 4				Network 5				Network 6			
Output MFs	Constant		Linear		Constant		Linear		Constant		Linear	
Inputs MFs	Check	Train	Check	Train	Check	Train	Check	Train	Check	Train	Check	Train
Trimf	0.063	0.047	0.005	0.004	0.161	0.111	0.008	0.006	1.16	0.927	0.028	0.018
Trapmf	0.077	0.053	0.022	0.012	0.126	0.18	0.071	0.04	1.508	0.953	0.439	0.241
Gbellmf	0.07	0.048	0.008	0.005	0.126	0.115	0.018	0.071	1.251	0.796	0.089	0.05
Gaussmf	0.066	0.047	0.005	0.003	0.132	0.108	0.007	0.005	1.205	0.833	0.034	0.02
Gauss2mf	0.076	0.067	0.013	0.018	0.13	0.189	0.036	0.022	1.526	0.948	0.176	0.127
Pimf	0.087	0.06	0.026	0.014	0.153	0.221	0.076	0.042	1.72	1.08	0.436	0.238
Dsigmf	0.076	0.052	0.01	0.006	0.127	0.12	0.032	0.02	1.145	0.935	0.162	0.099
Psigmf	0.076	0.052	0.009	0.006	0.127	0.12	0.032	0.019	1.144	0.935	0.158	0.09

Table 6 ANFIS training errors

	RMSE	MSE	MAE	R^2	$\overline{e_i}$	Std
Network1	0.0169	0.0002	0.0093	0.9995	0.0004	0.097
Network2	0.0219	0.0004	0.0170	1	−0.0005	0.0220
Network3	0.0729	0.0053	0.0417	1	0.0018	0.0733
Network4	0.0039	0.00001	0.0030	0.999	0.0003	0.0039
Network5	0.0066	0.0004	0.0051	1	−0.0003	0.0066
Network6	0.0205	0.00042	0.0131	1	0.0002	0.0205

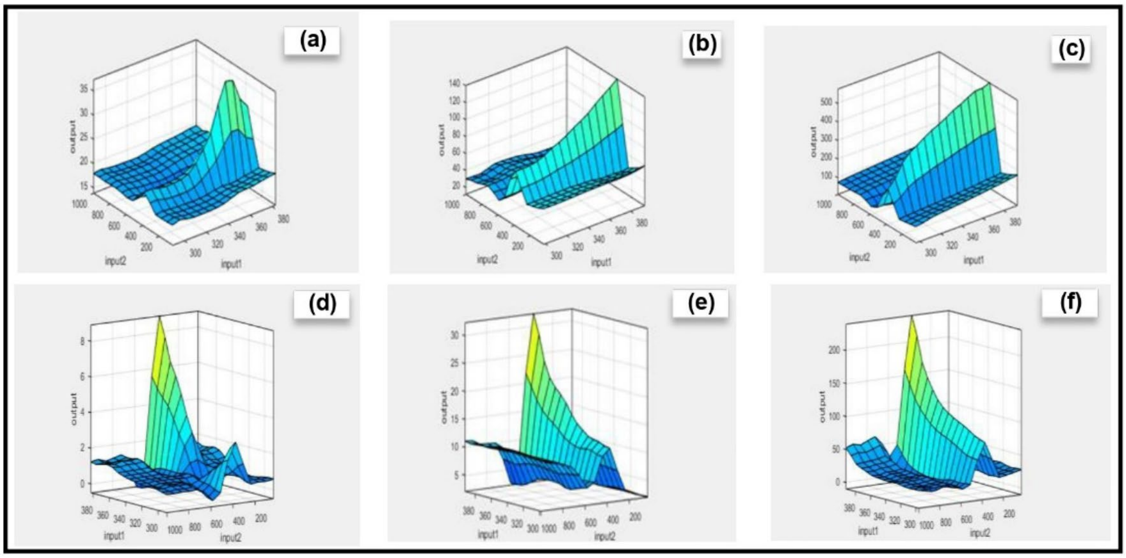

Fig. 9 Three dimensions ANFIS surface Representation between two inputs and output

predictions for experimentally observed values as well as forecasts for experimentally unmeasured values. At 150 kHz, predictions for values that were empirically measured were processed. This prediction is made as a testing phase to enable comparison of the anticipated ANFIS findings with the experimental results, indicating great agreement with the experimental results, and ensuring the model's effectiveness. The prediction for

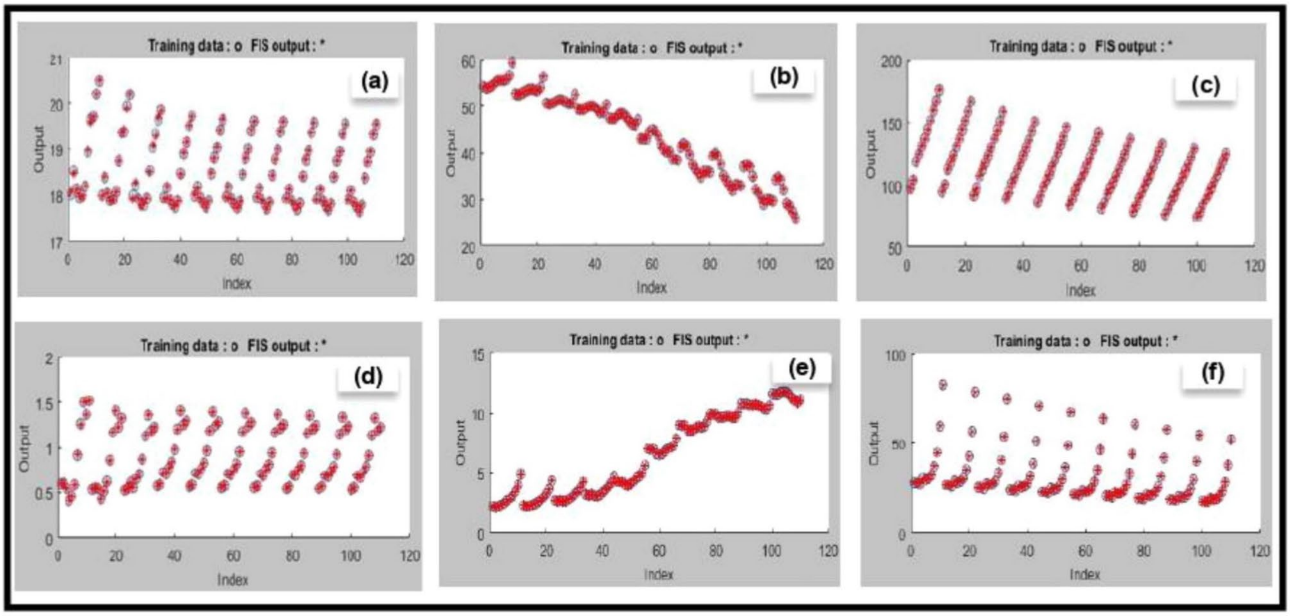

Fig. 10 Error Analysis between Training Data & FIS Output for ANFIS networks Models

unmeasured values is processed at 1500 kHz and 2000 kHz. Figure 11a–c shows the ANFIS modeling results for ε_1 (ω) and Fig. 11d–f shows the ANFIS modeling results for ε_2 (ω) as a function of temperature T (K) at different frequencies, respectively.

4 Conclusion

In conclusion, the analysis of dielectric properties offers significant value in studying the relationship between materials' electrical characteristics, temperature, and frequency. It provides information about the capacitive and conductive nature of materials through parameters such as dielectric (constant (ε_1) and loss (ε_2)), the observed decreasing trend in (ε_1) and (ε_2) with increasing audio frequency may be due to various polarization mechanisms, including electronic, ionic, dipolar, and space charge polarizations. Ionic polarization has minimal influence on overall polarization in the investigated compositions due to its covalent nature. The increase in ε_1 with temperature is explained by the facilitated orientation of dipoles in polar materials as the temperature rises. The addition of Ge and Te to the Se–Bi binary composition leads to an increase in ε_1, with a higher increase observed for Ge. This can be attributed to the stronger bonding between Se and Ge, which enhances the response to an electric field. The correlation between dielectric constant and AC conductivity is represented by the figure of merit parameter M, where higher M values indicate suitability for solar cell applications. Regarding dielectric loss (ε_2), the decrease in frequency results in a reduction due to the migration of ions in the material, which is the primary reason for dielectric loss at lower frequencies. Conversely, at higher frequencies, the main contributor to dielectric loss is the vibrations of ions. Additionally, ε_2 increases with temperature along with the increase in AC conduction loss. Overall, the dielectric analysis provides valuable insights into the electrical behavior of materials, aiding in their characterization and potential applications in various fields such as electronics and energy conversion. The ANFIS model is effective at modeling and estimating the dielectric characteristics of Se83Bi17 (SB), $Se_{83}Bi_{17}Te_5$ (SB-T), and $Se_{83}Bi_{17}Ge_5$ (SB-G), with the lowest mean errors. Also, Error Analysis between Training Data & FIS Output for ANFIS network Models is within acceptable limits. The modeling ANFIS results and the accompanying experimental data show excellent agreement. Dielectric characteristic values for frequencies of 150 kHz, 1500 kHz, and 2000 kHz were expected. The aforementioned projected values are not empirically measured, but the prediction ANFIS findings are processed and yield satisfactory results.

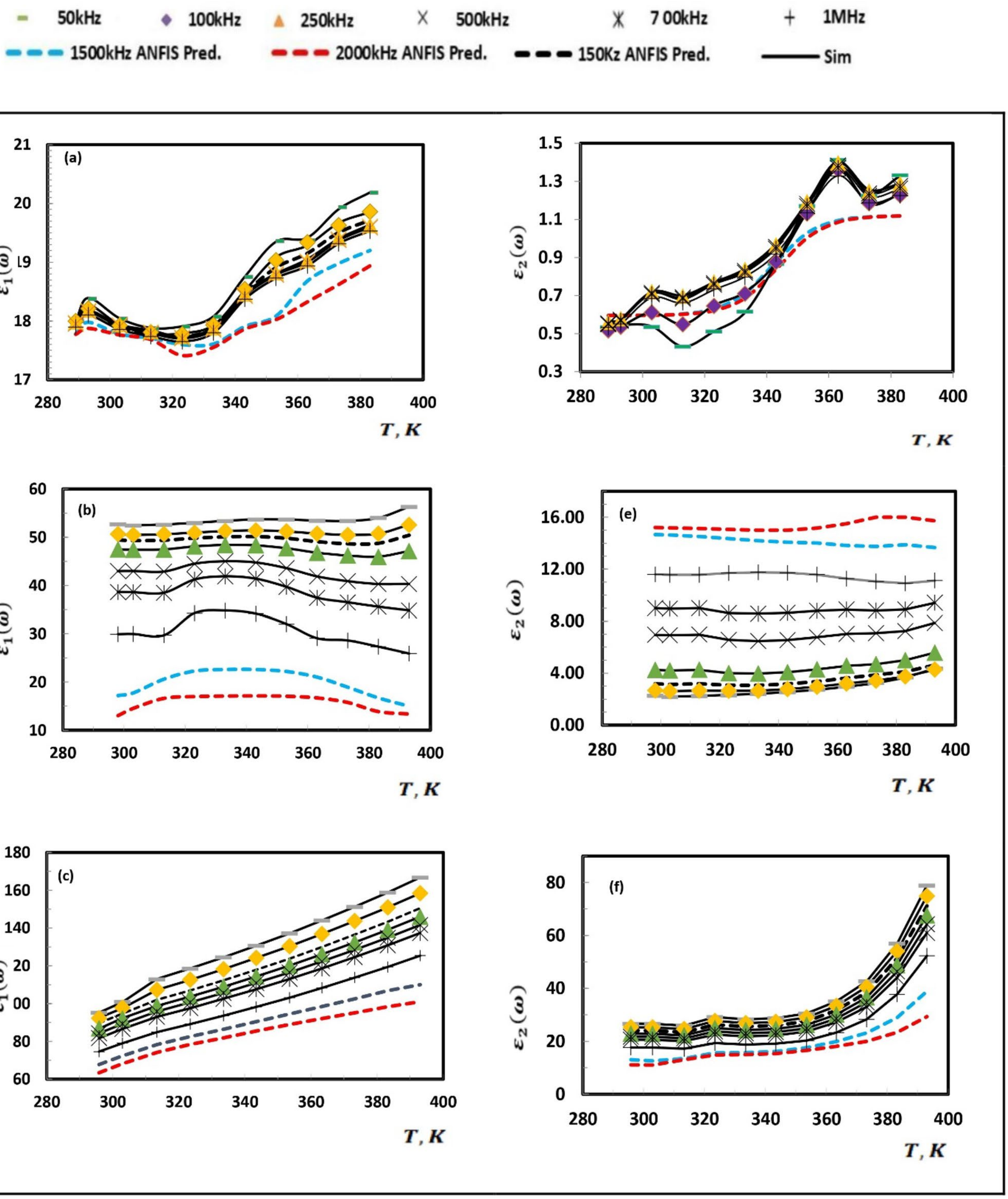

Fig. 11 Comparison between experimental data for dielectric constant (ε_1) (**a**, **b**, **c**), and for dielectric loss (ε_2) (**d**, **e**, **f**), respectively, as a function of temperature for glassy thin films of $Se_{83}Bi_{17}$ (SB), $Se_{83}Bi_{17}Te_5$ (SB-T), and $Se_{83}Bi_{17}Ge_5$ (SB-G) samples, respectively, (ANFIS) results containing simulated and predicted outputs for different frequencies

Author contributions

H. I. Lebda contributed to the concept's formulation, writing, software, formal analysis, collecting data, editing, and first draft review; H. E. Atyia contributed to the conception, carried out the experiments, analyzed the findings, wrote the manuscript, collected data, edited it, and revised it; D.M. Habashy participated in putting the idea, writing, software, formal analysis, data collection, editing, and reviewing the manuscript.

Funding

Open access funding provided by The Science, Technology & Innovation Funding Authority (STDF) in cooperation with The Egyptian Knowledge Bank (EKB).

Data availability

All the data that support the findings of this study are included in the article.

Declarations

Conflict of interest The author declares that there is no conflict of interest.

References

1. J.R. Smith, A.B. Johnson, Electrical properties of selenium-based compounds. J. Appl. Phys. **145**(3), 034701 (2018). https://doi.org/10.1063/1.5000001
2. C.D. Anderson, R.K. Patel, Bismuth-based materials for electronic applications. Mater. Sci. Eng. R. Rep. **138**, 1–22 (2019). https://doi.org/10.1016/j.mser.2019.01.001
3. S. Lee, H. Kim, T. Park, Influence of germanium and tellurium additions on the electrical behavior of Se-Bi compounds. J. Mater. Sci. **55**(15), 6782–6795 (2020). https://doi.org/10.1007/s10853-020-04994-1
4. R. Gupta, A. Kumar, D. Singh, Dielectric properties of Se-Bi-Ge glasses. J. Non-Cryst. Solids **471**, 93–98 (2017). https://doi.org/10.1016/j.jnoncrysol.2017.06.008
5. Z. Zheng, M. Li, J. Li, X. Zhang, Investigation of electrical properties in Se-Bi-Te glasses. J. Mater. Sci. Mater. Electron. **30**(4), 3974–3980 (2019). https://doi.org/10.1007/s10854-018-0075-9
6. K. Sangeetha, A. Arun, S.P. Kumar, Influence of composition on the electrical and thermal properties of Se-Bi-Ge-Te glasses. J. Alloy. Compd. **816**, 152582 (2020). https://doi.org/10.1016/j.jallcom.2019.152582
7. S. Das, A. Ghosh, Study of electrical and dielectric properties of Se-Bi-Ge and Se-Bi-Te thin films. J. Mater. Sci. Mater. Electron. **32**(1), 464–473 (2021). https://doi.org/10.1007/s10854-020-04284-0
8. G.M. El- Damrawi, M.A. Abdel-Rahim, A.A. El-Sayed, Electrical properties of Se-Bi-Ge alloy thin films for potential electronic applications. J. Electron. Mater. **51**(1), 335–344 (2022). https://doi.org/10.1007/s11664-021-09229-3
9. H.E. Atyia, Effect of annealing temperature on the electric and dielectric properties of Se70Te15Bi15 films. Acta Phys. Polonica A **125**, 98–104 (2014)
10. H.E. Atyia, Electrical conductivity and dielectric relaxation of bulk Se70Bi(30–x)Tex, x = (0, 15) chalcogenide glasses. J. Non-Cryst. Solids **391**, 83–90 (2014)
11. D.M. Habashy, M.Y. El-Bakry, E.A. El-Dahshan, H.I. Lebda, Artificial intelligence approaches for studying the *pp* interactions at high energy using adaptive neuro-fuzzy interface system. Neuromorphic Computing (2023). https://doi.org/10.5772/intechopen.111552
12. D.M. Habashy, H.A.M. Ali, Performance analysis of adaptive neuro-fuzzy inference-based relying on modeling electric modulus feature of 3-formylchromone. Mater. Sci. Semicond. Process. **165**, 107659 (2023)
13. M.N. Shahrak, M. Esfandyari, M. Karimi, Efficient prediction of water vapor adsorption capacity in porous metal–organic framework materials: ANN and ANFIS modeling.

J. Iran. Chem. Soc. **16**, 11–20 (2019). https://doi.org/10.1007/s13738-018-1476-.y

14. M. Jalal, A.A. Ramezanianpour, A.R. Pouladkhan, P. Tedro, Application of genetic programming (GP) and ANFIS for strength enhancement modeling of CFRP-retrofitted concrete cylinders. Neural Comput. Appl. **23**, 455–470 (2013). https://doi.org/10.1007/s00521-012-0941-2
15. S.T. Kumaran, T.J. Ko, R. Kurniawan, C. Li, M. Uthayakumar, ANFIS modeling of surface roughness in abrasive waterjet machining of carbon fiber reinforced plastics. J. Mech. Sci. Technol. **31**(8), 3949–3954 (2017). https://doi.org/10.1007/s12206-017-0741-9
16. D. Petković, M. Barjaktarovic, S. Milošević, N. Denić, B. Spasić, J. Stojanović, M. Milovancevic, Neuro fuzzy estimation of the most influential parameters for Kusum biodiesel performance. Energy **229**, 120621 (2021). https://doi.org/10.1016/j.energy.2021.120621
17. D. Petković et al., Application of distance learning in mathematics through adaptive neuro-fuzzy learning method. Comput. Electr. Eng. **93**, 107270 (2021). https://doi.org/10.1016/j.compeleceng.2021.107270
18. B. Kuzman, B. Petković, N. Denić, D. Petković, B. Ćirković, J. Stojanović, M. Milić, Estimation of optimal fertilizers for optimal crop yield by adaptive neuro fuzzy logic. Rhizosphere **18**, 100358 (2021). https://doi.org/10.1016/j.rhisph.2021.100358
19. N. Lakovic, A. Khan, B. Petkovic, D. Petkovic, B. Kuzman, S. Resic, K. Jermsittiparsert, S. Azam, Management of higher heating value sensitivity of biomass by hybrid learning technique. Biomass Convers Biorefinery (2021). https://doi.org/10.1007/s13399-020-01223-w
20. M. Milic, B. Petkovic, A. Selmi, D. Petkovic, K. Jermsittiparsert, A. Radivojevic, M. Milovancevic, A. Khan, S.T. Vidosavljevic, N. Denic, B. Kuzman, Computational evaluation of microalgae biomass conversion to biodiesel. Biomass Convers Biorefinery (2021). https://doi.org/10.1007/s13399-021-01314-2
21. V. Nikolic, D. Petkovic, L. Lazov, M. Milovancevic, Selection of the most influential factors on the water-jet assisted underwater laser process by adaptive neuro-fuzzy technique. Infrar. Phys. Technol. **77**, 45–50 (2016). https://doi.org/10.1016/j.infrared.2016.05.021
22. D. Petkovic, M. Gocic, S. Trajkovic, M. Milovanˇcevic, D. Ševic, Precipitation concentration index management by adaptive neuro-fuzzy methodology. Clim. Change **141**, 655–669 (2017). https://doi.org/10.1007/s10584-017-1907-2
23. S. Akkoyun, Y. Torun, Neuro-fuzzy modeling of deformation parameters for fusion-barriers. Nucl. Eng. Technol. **53**(5), 1612–1618 (2021). https://doi.org/10.1016/j.net.2020.10.017
24. D. Petković et al., Adaptive neuro-fuzzy maximal power extraction of wind turbine with continuously variable transmission. Energy **64**, 868–874 (2014). https://doi.org/10.1016/j.energy.2013.10.094
25. D. Petkovic, S.H. Abhamid, Z. Cojbasic, N.D. Pavlovi, Adapting project management method and ANFIS Strategy for variables selection and analyzing wind turbine wake effect. Nat. Hazards **74**, 463–475 (2014). https://doi.org/10.1007/s11069-014-1189-1
26. V. Nikolić, V.V. Mitić, L. Kocić, D. Petković, Wind speed parameters sensitivity analysis based on fractals and neuro-fuzzy selection technique. Knowl. Inf. Syst. **52**, 255–265 (2017). https://doi.org/10.1007/s10115-016-1006-0
27. N.T. Thinh, D.T. Dung, Adaptive neuro-fuzzy control for ionic polymer metal composite actuators, in Robot Intelligence Technology and Applications 2, Advances in Intelligent Systems and Computing, vol. 274, edited by J.H. Kim et al. (2014) 939–947. https://doi.org/10.1007/978-3-319-05582-4_82
28. D.M. Habashy, H.A.M. Ali, Performance analysis of adaptive neuro-fuzzy inference-based relying on modeling electric modulus feature of 3-formylchromone. Mater. Sci. Semicond. Process. **165**, 107659 (2023). https://doi.org/10.1016/j.mssp.2023.107659
29. D. Arcos-Aviles, J. Pascual, F. Guinjoan, L. Marroyo, G. García-Gutiérrez, R. Gordillo-Orquera, J. Llanos-Proaño, P. Sanchis, T.E. Motoasca, An energy management system design using fuzzy logic control: smoothing the grid power profile of a residential electro-thermal microgrid. IEEE Access **9**, 25172–25188 (2021). https://doi.org/10.1109/ACCESS.2021.3056454
30. M. Gaber, S. El-Banna, M. El-Dabah, M. Hamad, Designing and implementation of an intelligent energy management system for electric ship power system based on adaptive neuro-fuzzy inference system. Adv. Sci., Technol. Eng. Syst. J. **6**(2), 195–203 (2021). https://doi.org/10.25046/aj060223
31. M. Babanezhad, A. Masoumian, A. Taghvaie Nakhjiri, A. Marjani, S. Shirazian, Influence of number of membership functions on prediction of membrane systems using adaptive network based fuzzy inference system (ANFIS). Sci. Rep. **10**, 16110 (2020)
32. H.E. Atyia, A.S. Farid, Non-isothermal crystallization kinetics of ternary Se90Te10-xPbx glasses. J. Cryst. Growth **436**, 125 (2016). https://doi.org/10.1016/j.jcrysgro.2015.12.004
33. H.E. Atyia, N.A. Hegab, Dielectric relaxation behavior and conduction mechanism of Te46As32Ge10Si12 films.

Optik **127**, 6232–6242 (2016). https://doi.org/10.1016/j.ijleo.2016.04.024

34. R. Larson, B. Farber, Picturing the World, Prentice-Hall, Englewood Cliffs, NJ, 2003.
35. D.Moore, G.McCabe, W.H. Freeman and Co., London, 2003.
36. J.S. Wang, C X Ning ANFIS based time series prediction method of bank cash flow optimized by adaptive population activity PSO algorithm. Information **6**, 300 (2015). https://doi.org/10.3390/info6030300
37. Tarno, Subanar, D. Rosadi, Suhartono Analysis of financial time series data using adaptive neuro-fuzzy inference system (ANFIS) International Journal of Computer Science Issues. 10, 491 (2013). ISSN (Online): 1694–0784
38. M. Babanezhad, I. Behroyan, A.T. Nakhjiri, A. Marjani, S. Shirazian, Performance and application analysis of ANFIS artificial intelligence for pressure prediction of nanofluid convective flow in a heated pipe. Sci. Rep. **11**, 902 (2021). https://doi.org/10.1038/s41598-020-79628-w
39. N. Talpur, M.N. Mohd Salleh, K. Hussain, An investigation of membership functions on performance of ANFIS for solving classification problems. Mater. Sci. Eng.. **226**, 012103 (2017). https://doi.org/10.1088/1757-899X/226/1/012103
40. S.O. Sada, S.C. Ikpeseni, Evaluation of ANN and ANFIS modeling ability in the prediction of AISI 1050 steel machining performance. Heliyon **7**, e06136 (2021). https://doi.org/10.1016/j.heliyon.2021.e06136
41. N.A. Hegab, M.A. Afifi, H.E. Atyia, A.S. Farid, ac conductivity and dielectric properties of amorphous Se80Te20−xGex chalcogenide glass film compositions. J. Alloy. Compd. **477**, 925–930 (2009). https://doi.org/10.1016/j.jallcom.2008.11.129
42. S. Ojha, M. Sahidul Ali, M. Roy, S. Bhattacharya, Hopping frequency and conductivity relaxation of promising chalcogenides: AC conductivity and dielectric relaxation approaches. Mater. Res. Express **8**, 085203 (2021). https://doi.org/10.1088/2053-1591/ac1d17
43. M.M. Bouzayani, M. Ben Abdessalem, I. Soudani, A. Oueslati, A. Aydi, Influence of potassium doping on the structural, conduction mechanism, and dielectric properties of CaFe2O4. RSC Adv **14**, 12464–12474 (2024). https://doi.org/10.1039/d4ra00260a
44. S.S. Fouad, B. Parditka, H.E. Atyia, E. Baradacs, A.E. Bekheet, Z. Erdelyi, AC conductivity and dielectric parameters studies in multilayer TiO2/ZnO thin films produced via ALD technique. Chin. J. Phys. **77**, 73–80 (2022). https://doi.org/10.1016/j.cjph.2022.02.001
45. S.S. Fouad, B. Parditka, H.E. Atyia, E. Baradács, Z. Erdelyi, The real role of Cu metallic interlayer on the dielectric dispersion and conduction mechanism of TiO2/Cu/TiO2 nanolaminates. Optik **260**, 169078 (2022). https://doi.org/10.1016/j.ijleo.2022.169078
46. K.J. Hamam, G. Mezei, Z. Khattari, M. Maghrabi, F. Afaneh, W.A. Al Isawi, F. Salman, Temperature and frequency effect on the electrical properties of bulk nickel phthalocyanine octacarboxylic acid (Ni-Pc(COzOH)8). Appl. Phys. A **125**, 7 (2019). https://doi.org/10.1007/s00339-018-2147-7
47. H.E. Atyia, N.A. Hegab, M.A. Affi, M.I. Ismail, Influence of temperature and frequency on the AC conductivity and dielectric properties for Ge15Se60Bi25 amorphous films. J. Alloy. Compd. **574**, 345–353 (2013). https://doi.org/10.1016/j.jallcom.2013.04.155
48. Z. Tang, Y. Liu, Y. Du, Frequency dependence of dielectric loss in thin film composites. J. Mater. Sci. Mater. Electron. **31**(5), 4146–4153 (2020)
49. D.M. Habashy, H.E. Atyia, H.I. Lebda, Exploring conduction mechanisms in chalcogenide thin films: an experimental and soft computing approach with ANN and GP techniques. Eur. Phys. J. Plus **138**, 798 (2023). https://doi.org/10.1140/epjp/s13360-023-04382-7
50. Q. Zhang, X. Wang, Investigation of dielectric loss in glassy films at different temperatures. J. Mater. Sci. **54**(18), 12065–12074 (2019)